1

1   **Revision 1**

2

3

The Crystal Structure of Feitknechtite (β-MnOOH)

and a new MnOOH Polymorph

6

7   Jeffrey E. Post[1]*, Peter J. Heaney[2], Eugene S. Ilton[3], and Evert J. Elzinga[4]

8   *[1]Department of Mineral Sciences, Smithsonian Institution, PO Box 37012, Washington, DC*
9   *20013-7012, United States*
10   *[2]Department of Geosciences, Penn State University, University Park, PA 16802, United States*

11   *[3]Pacific Northwest National Laboratory, 902 Battelle Blvd, Richland, WA 99352, United States*

12   *[4]Department of Earth & Environmental Sciences, Rutgers University, Newark, New Jersey*
13   *07102, United States*

14

15

16

17

18   *[*]To whom correspondence should be addressed:* postj@si.edu

19

ABSTRACT

20

21   Studies suggest that feitknechtite (β-MnOOH) is a prevalent, and perhaps necessary,

22   intermediate phase during the synthesis of birnessite-like phases, the abiotic oxidation of Mn^{2+},

23   and the transformation of biogenic hexagonal phyllomanganates to more complex Mn oxides in

24   laboratory and natural systems. Researchers have generally described feitknechtite as consisting

25   of pyrochroite-like (or cadmium iodide-like) Mn-O octahedral layers, but a detailed crystal

26   structure has not been reported. We used TEM/SAED and powder XRD and Rietveld

27   refinements to derive the unit cell and, for the first time, report a complete structure description

28   for feitknechtite (β-MnOOH). Rietveld refinements were also completed for three natural

29   feitknechtite/hausmannite samples, and time-resolved synchrotron XRD experiments were used

30   to follow the thermal transformation of feitknechtite to hausmannite. Additionally, we identified

31   and report the structure for a second, and perhaps novel, MnOOH polymorph (proposed

32   designation - ε-MnOOH), mixed with the synthetic feitknectite, that is similar to β-MnOOH but

33   with a different layer stacking.

34

35

INTRODUCTION

36

37   Feitknecht and Marti (1945) observed that oxidation of a suspension of synthetic

38    $Mn(OH)_2$ resulted in a hydrated oxide of tri- and divalent Mn with a crystal structure related to

39   that of hausmannite (Mn_3O_4). The hydrate was distinguished from hausmannite by the presence

40   of a strong extra line (of unspecified d-spacing – only a line drawing was shown) in the low-

41   angle region of the powder diffraction pattern. Frondel (1953) described a natural analogue of

42   this same hydrous Mn oxide as an alteration product of natural $Mn(OH)_2$ (pyrochroite) crystals

43   from Sweden and Franklin, NJ. He called this new mineral hydrohausmannite, the same name

44   proposed by Feitknecht and Marti (1945) for their synthetic material. Frondel (1953) also

45   observed the same characteristic low-angle strong line noted by Feitknecht and Marti (1945) in

46   the powder XRD pattern, and Frondel (1963) reported the d-spacing as 4.65 Å. Electron

47   microscopy studies by Feitknecht et al. (1962), however, revealed that synthetic

48   hydrohausmannite was actually a mixture of Mn_3O_4 (hausmannite) and a second phase that they

49   called β-MnOOH. Bricker (1965) examined a hydrohausmannite sample from Sweden and

50   confirmed that it too was a mixture of the same two phases. He proposed that β-MnOOH be

51   given the mineral name feitknechtite and that hydrohausmannite be discredited.

52   Synthesis experiments by Bricker (1965) suggested that a series of compounds might

53   exist spanning the composition range from $Mn(OH)_2$ to MnOOH. They observed that a mixture

54   of β-MnOOH and hausmannite always formed from rapid oxidation of water suspensions of

55    $Mn(OH)_2$, and that the solids transform to manganite (γ-MnOOH) upon standing. Hem et al.

56   (1978, 1982) similarly report that β-MnOOH is the phase commonly obtained when Mn^{2+} is air-

57   oxidized, but that it is metastable and changes to manganite on aging in aerated solutions. They

58   also suggested that it is an important intermediate for various Mn oxidation reactions,

59   particularly in natural systems at temperatures < 20 °C, where aqueous systems might first form

60   feitknechtite as the precursor to MnO_2 phases, e.g., lake and ocean nodules. Klewicki and

61   Morgan (1999) concluded that dissolution of MnOOH phases by Mn(III)-stabilizing ligands

62   (e.g., citrate, EDTA, and pyrophosphate) at circumneutral pH conditions might be a significant

63   factor in Mn cycling in natural waters.

64   Many researchers have suggested that Mn oxides in natural systems derive from biogenic

65   oxidation of dissolved Mn^{2+}, or by alteration of biogenic hexagonal birnessite-like phases to

66   more crystalline secondary oxides. For example, Mandernack et al. (1995) observe that

67   oxidation of aqueous Mn^{2+} by spores of *Bacillus* bacterium, strain SG-1, in HEPES-buffered

68   water and seawater systems, pH 7.4-8.0, produce predominantly hausmannite and feitknechtite at

69   high Mn^{2+} concentrations (> ~1 mM), whereas feitknechtite is favored at temperatures < ~25 °C.

70   Luo et al. (1998) report that feitknechtite is an intermediate phase initially formed during

71   synthesis of birnessite-like material via oxidation of $Mn(OH)_2$ with permanganate and acetate.

72   Barger et al (2005) demonstrate that biogenic hexagonal birnessite reacts with Mn^{2+} to form

73   triclinic birnessite-like phases for $[Mn^{2+}]$ < 500 μM but forms feitknechtite at higher

74   concentrations at near neutral pH. Elzinga (2011) and Lefkowitz et al. (2013) determined that

75   dissolved Mn^{2+} converts hexagonal birnessite-like phases to feitknechtite and manganite at

76   neutral pH and above, but that only feitknechtite forms at pH 7 to 8.5 for low Mn^{2+}

77   concentrations (274 μM). Elzinga (2011) suggests that feitknechtite is the first mineral to form

78   from the comproportionation reaction, $Mn^{2+} + Mn^{4+}O_2 + 2H_2O = 2Mn^{3+}OOH + 2H^+$, and he

79   argues that feitknechtite is a necessary precursor to the more stable manganite. Lefkowitz et al.

80   (2013) observe that feitknechtite also forms by autocatalytic oxidation of Mn^{2+} by O_2 in solution

81   and by surface oxidation of Mn^{2+} by O_2 on goethite and hematite surfaces, and they conclude

82   that feitknechtite is an important metastable Mn oxide phase in geochemical systems exhibiting

83   abiotic Mn^{2+} oxidation. Moreover, β-MnOOH is commonly observed as an intermediate during

84   the materials synthesis of Mn oxides, such as manganite nanowires (Portehault et al. 2010).

85   β-MnOOH (feitknechtite) is one of three naturally occurring MnOOH polymorphs, along

86   with α-MnOOH (groutite) and γ-MnOOH (manganite). Yamamoto et al. (1981) report

87   synthesizing a fourth polymorph, δ-MnOOH. Bricker (1965) infers that the structure of β-

88   MnOOH is closely related to that of brucite-like pyrochroite ($Mn(OH)_2$), but with a decrease of

89   the basal spacing from 4.72 to 4.62 Å as a consequence of the oxidation of Mn^{2+} to Mn^{3+}.

90   Various researchers have described feitknechtite as consisting of pyrochroite-like (or cadmium

91   iodide-like) Mn-O octahedral layers (Feitknecht et al. 1962; Bricker 1965; Meldau et al. 1973;

92   Mandernack et al. 1995; Portehault et al. 2010; Grangeon et al. 2017), but a detailed crystal

93   structure has not been reported. Bricker (1965) proposed a tetragonal unit cell with $a = 8.6$ Å

94   and $c = 9.3$ Å, whereas Mandernack et al. (1995) and Portehault et al. (2010) report powder XRD

95   patterns for feitknechtite that were similar to each other but different from that of Bricker (1965).

96   Meldau et al. (1973) conclude that feitknechtite is an isotype of pyrochroite and propose a

97   trigonal unit cell similar to that phase. Chukanov et al. (2021) also assume a trigonal unit cell

98   with $a = 3.32$ Å and $c = 4.71$ Å . Based on selected area electron diffraction patterns and XRD

99   data, Portehault et al. (2010) propose a monoclinic unit cell that is close to that determined for

100   synthetic Na-birnessite by Post and Veblen (1990).

101   The studies above suggest that feitknechtite (β-MnOOH) is a prevalent, and perhaps

102   necessary, intermediate phase to promote the precipitation of birnessite-like phases during the

103   abiotic oxidation of Mn^{2+} and the transformation of biogenic hexagonal phyllomanganates to

104   more complex Mn oxides in laboratory and natural systems. In light of this potentially critical

105 role, a better understanding is required of the atomic structure of feitknechite to model its

106 chemical reactivity, thermodynamic stability, and phase transformation pathways. For the current

107 study, we used TEM/SAED and powder XRD and Rietveld refinements to derive the unit cell

108 and, for the first time, the detailed atomic structure for feitknechtite (β-MnOOH). We also

109 present Rietveld refinements for three natural feitknechtite/hausmannite samples, and we

110 describe the thermal transformation of feitknechtite to hausmannite based on temperature-

111 resolved synchrotron XRD.

SAMPLES AND METHODS

Sample Description

114   Synthetic samples of β-MnOOH were prepared by reacting a synthetic hexagonal

115 birnessite-like phase with 274 μM Mn^{2+} solution at near-neutral pH (Elzinga et al. (2011). In

116 addition, we investigated three natural samples of feitknechtite and hausmannite after

117 pyrochroite from the Wessels Mine, South Africa, Långban, Sweden (NMNH B7731), and

118 Franklin, NJ (NMNH R2205).

Scanning Electron Microscopy (SEM)

120   Back-scattered electron (BSE) imaging, using a GAD detector, and energy-dispersive

121 spectrometry (EDS) X-ray analyses were carried out in the low-vacuum mode using a scanning

122 electron microscope (FEI Nova NanoSEM 600; Department of Mineral Sciences, Smithsonian

123 Institution) for powder samples of synthetic and natural feitknechtite dispersed onto a carbon

124 substrate. EDS analyses were performed on uncoated samples using 15 keV accelerating voltage.

125

126

Fourier transform infrared spectroscopy (FTIR)

127

128   Samples were disaggregated under acetone in a mortar and pestle and sieved through a

129   325 mesh (< 44 μm) sieve. Then, 0.5 mg of synthetic feitknechtite was milled with ~250 mg

130   KBr using a SPECAC ball mixing mill for 1-2 min and pressed into a pellet. Transmission

131   vibrational spectra were collected on a Nicolet 6700 Analytical FTIR Spectrometer for a range of

132   400 to 4000 cm^{-1}. The resolution was set at 3.86 cm^{-1} and 64 scans were co-added for each

133   spectrum. The background spectrum was collected using a KBr blank pellet. The Omnic 8

134   software (Nicolet) was used to view data during data collection.

Transmission Electron Microscopy (TEM)

135

136   Powdered samples of the synthetic and the South African feitknechtite were suspended in

137   ethanol and dispersed onto holey carbon copper TEM grids. Selected area electron diffraction

138   (SAED) and high-resolution transmission electron microscope (HRTEM) analyses were

139   performed with a Philips 420 TEM and an FEI Talos F200X (S)TEM using acceleration voltages

140   of 120 kV and 200 kV, respectively, at the Materials Characterization Laboratory, Penn State

141   University. Simulations of selected area electron diffraction patterns were calculated using

142   SingleCrystal software (CrystalMaker Software Ltd.).

X-ray photoelectron spectroscopy (XPS)

143

144   For XPS analysis, data collection and fitting procedures were followed as reported by

145   Ilton et al. (2016). A powder sample of the synthetic feitknechtite was mounted on a strip of

146   conductive copper tape affixed to a copper stub and then pressed with a clean borosilicate glass

147   block. Measurements were conducted with a Kratos Axis Ultra DLD spectrometer with an Al

148   *Kα* X-ray source (1486.7 eV) operating at 10 mA and 15 kV. Magnetic immersion lenses were

149 used to improve collection efficiency. The instrument work function was calibrated to give a

150 binding energy (BE) of 83.96 eV ± 0.05 eV for the $4f_{7/2}$ line of metallic gold. The spectrometer

151 dispersion was adjusted to yield a BE of 932.62 eV for the Cu$2p_{3/2}$ line of metallic copper.

152 Measurements of the Mn$2p$, Mn$3s$, Mn$3p$, and O$1s$, lines were conducted with a step size of 0.1

153 eV, an analysis area of 300 x 700 μm, and pass energies (PE) of 20 or 40 eV. The resultant full-

154 width-at-half-maximums (FWHM) for the Ag$3d_{5/2}$ line were 0.54 and 0.77 eV, respectively. The

155 low sensitivity of the Mn$3s$ line resulted in measurements only with PE = 40 eV. Survey scans

156 were conducted at PE = 160 eV and step size = 0.5 eV. XPS spectra were fit by non-linear least

157 squares after Shirley background subtractions with the CasaXPS curve resolution software

158 package. Gaussian/Lorentzian contributions to line shapes were numerically convoluted with a

159 Voigt function.

160 **X-ray Diffraction and Rietveld Refinement**

161   The samples used for X-ray diffraction were hand ground under acetone in an agate mortar

162 and passed through a 325-mesh sieve and loaded into 0.7 mm quartz-glass or 1 mm (ID)

163 polyimide (APS) capillaries. XRD data for the synthetic sample were collected: 1) at the

164 Advanced Photon Source (APS) GeoSoilEnviroCARS (GSECARS) 13-BM-C beam line, using

165 0.83154 Å radiation and a CCD detector, and 2) at the APS high-resolution XRD beamline

166 11BM, using a wavelength of 0.414211 Å. Conventional XRD data for the mineral samples

167 were collected using a Rigaku DMAX-Rapid diffractometer (Smithsonian Institution), with a

168 curved imaging plate, using Mo radiation. A LaB$_6$ powder (NIST SRM660a) was used to

169 calibrate experimental instrument parameters. Preferred orientation of the powder was

170 eliminated through a combination of specimen rotation, use of a capillary sample holder, and full

171 intensity integration of the diffraction rings, as obtained using the program Dioptas (Prescher and

172   Prakapenka 2015) (APS data) or 2DP (Rigaku) for the Mo radiation patterns, with a polarization

173   factor of 0.99.

174   High temperature XRD of β-MnOOH was performed at the APS 13-BM-C beamline with

175   an X-ray wavelength of 0.83154 Å. Synthetic feitknechtite powder was loaded into a 0.7 mm

176   thin-walled quartz capillary with one end unsealed to release water when heating. An electrically

177   resistive forced air heater, using He as the transport gas, was placed directly below the capillary,

178   and temperature was measured using a thermocouple, which was calibrated through phase

179   transitions of $RbNO_3$, yielding an estimated temperature error of ±1.5 °C. Temperature-resolved

180   data from 25 to 424 °C were collected as a series of 15 s exposures at 3 °C increments. During

181   each exposure, the sample was rotated through a 75° angle.

182   Indexing of the powder X-ray diffraction peaks and Rietveld refinements (Rietveld, 1969)

183   were performed using the General Structure Analysis System-II (GSAS-II) software (Toby and

184   Von Dreele 2013). Diffraction data generated by the LaB_6 standard (NIST SRM 660a) were used

185   to calibrate peak profile parameters that described instrumental broadening. For all samples,

186   diffraction peak profiles were fit with a pseudo-Voigt function as parameterized by Thompson et

187   al. (1987), and microstrain anisotropic broadening terms by Stephens (1999).

188

189   **Results**

190   **Structures of feitknechtite and MnOOH-Phase 2**

191   The high-resolution powder diffraction data (APS 11BM) were indexed by a monoclinic

192   *C*2/*m* unit cell with parameters given in Table 1. This unit cell successfully indexed all observed

193   diffraction peaks, except for several weak peaks (strongest < ~2.5% of the most intense

194   feitknechtite peak), e.g., at 2.82 Å, 2.55 Å, 2.24 Å, and 1.71 Å. Using GSASII, we were able to

195   index the extra weak reflections separately using a unit cell for which *a* and *b* were similar to

196   those of feitknechtite, but with a β angle close to 90° and *c* of ~4.60 Å (Table 1). Bricker (1965)

197   reported that his attempts to synthesize β-MnOOH from aqueous solution under a variety of

198   conditions always produced mixtures of Mn oxide phases, with impurities such as hausmannite

199   and other unidentified MnII/MnIII oxides. XRD patterns of the natural specimens from South

200   Africa, Franklin, and Sweden did not show the extra peaks for the impurity phase observed in

201   our synthetic sample. The unit-cell parameters determined for feitknechtite are close to those

202   measured from our TEM SAED patterns and to those determined from SAED patterns from

203   synthetic β-MnOOH by Portehault et al. (2010).

204   Based on the similarity of the feitknechtite unit-cell parameters to those of Na-birnessite

205   (Table 1), we selected initial Mn and O atom positions for the Rietveld refinement that were

206   similar to those in monoclinic Na-birnessite, as reported by Post and Veblen (1990), but adjusted

207   for the shorter *c* axis. Only background parameters, scale factor, unit-cell parameters, and peak

208   profile coefficients were varied in the initial refinement cycles; background intensities were

209   fitted with a Chebyshev function using 5-7 terms. The overall good fit to the observed pattern

210   confirmed that the basic structure model was correct.

211   The final refinement stages for the synthetic feitknechtite sample also included the

212   impurity phase, "MnOOH-Phase 2", using the unit cell determined by the indexing program. As

213   the unit cell indicated a layer structure similar to that of feitknechtite, but with a different β

214   angle, the same Mn and O positions as determined for feitknechtite were applied to the starting

215   structure model for Phase 2. Phase 2 fit the extra peaks well, and the R_{wp} goodness-of-fit

216   parameter improved from 0.175 to 0.117. The refinement for the synthetic mixture yielded

217   abundances of ~86 wt% feitknechtite and ~14 wt % Phase 2. After convergence, the O atom

218   positions for feitknechtite and Phase 2 were refined. Refinements of the feitknechtite Mn and O

219   occupancy factors yielded values that were not significantly different than 1.0 and were fixed at

220   unity.

221   The final refinement parameters and other structure details for RT synthetic feitknechtite

222   (β-MnOOH) and MnOOH-Phase 2, using the APS 11BM data, are given in the supplementary

223   CIF, and atom positions and selected bond distances are reported in Table 2. The final observed,

224   calculated, and difference X-ray diffraction patterns are plotted in Figure 1, and modeled and

225   observed SAED patterns for multiple zone axes are shown in Figure 2. Polyhedral structure

226   representations are shown in Figure 3.

227   The structure model determined above was successfully applied to the mineral samples

228   from South Africa, Sweden, and New Jersey. The unit-cell parameters are listed in Table 1. It

229   was also used for Rietveld refinements during the heating of the synthetic powders from RT to

230   424 °C. When present, the hausmannite phase was fit using starting structure parameters

231   reported by Baron et al. (1998).

232

233   **DISCUSSION**

234   **Comparison of the feitknechtite (β-MnOOH) structure with that of related Mn hydroxides**

235   As discussed above, because feitknechtite is readily formed by the oxidation of

236   pyrochroite, many researchers have assumed that its structure is some permutation of the

237   pyrochroite brucite-like structure (Aminoff 1919). A detailed structure description, however,

238   that includes unit-cell parameters and atom positions, has not previously been reported. Our

239   structure solution and refinement confirm that feitknechtite is constructed of parallel layers of

240   Mn^{3+}-(O,OH) octahedra, making it the only known purely Mn^{3+} layer structure. The Mn^{3+} Jahn-

241   Teller distortions for the Mn-(O,OH) octahedra result in elongated axial bonds [2.286(1) Å]

242   relative to the four equatorial distances [1.933(1) Å], similar to those observed in other Mn^{3+}

243   oxides, e.g., 2.28 and 1.93 Å, respectively, in hausmannite (Jarosch 1987). The calculated mean

244   Mn-O bond length of 2.05 matches well the values of 2.04 Å and 2.05 Å reported for <Mn-O>

245   bond distances in manganite (γ-MnOOH) and groutite (α-MnOOH), respectively, (Kohler et al.

246   1997) and of 2.05 Å for hausmannite (Baron et al. 1998). This observation is consistent with our

247   XPS data (below) showing that, within error, all Mn in our synthetic feitknechtite is trivalent.

248   The pronounced Jahn-Teller octahedral distortions reduce the structure symmetry from trigonal

249   in pyrochroite (S.G. $P\overline{3}m$) to monoclinic (S.G. $C2/m$).

250   Energy dispersive spectroscopy revealed only Mn and O in the synthetic sample. Charge

251   balance for the chemical formula MnOOH requires that half of the O atoms are OH⁻ anions, as in

252   the MnOOH polymorphs groutite and manganite, and indicated by FTIR (below). Single-crystal

253   refinements for groutite and manganite (Kohler et al. 1997) revealed a disparity in the Mn-O and

254   Mn-OH bond lengths, with Mn-OH longer for both axial and equatorial octahedral distances.

255   Oxygen and OH groups are disordered over the one symmetrically unique O atom site in

256   feitknechtite, and therefore cannot be distinguished. The O atoms at the base of an octahedral

257   sheet in feitknechtite are situated in nearly vertical alignment above the O atoms at the top of the

258   octahedral sheet below (Fig. 3). The O-O distance across the interlayer in feitknechtite is 2.80 Å,

259   which is typical for OH-O hydrogen bonds (Bauer 1972). This relationship suggests that the H

260   atoms are arranged such that OH at the base of one octahedral sheet will lie above O atoms at the

261   top of the adjacent sheet below. Consequently, some H atoms within an interlayer will be closer

262   to one sheet and some closer to the other in a disordered fashion. This network of H-bonds

263   across the interlayer binds the octahedral sheets tightly together, resulting in a closer layer

264   spacing of 4.62 Å in feitknechtite, as compared to 4.72 Å in $Mn(OH)_2$-pyrochroite (Bricker

265   1965)]. In groutite, the O1$\cdots$H2-O2 distance across the short dimension of the 1x2 octahedral

266   tunnels is 2.57 Å, accounting for its slightly smaller "layer spacing" (distance between parallel

267   double chains) of 4.557 Å (Kohler et al. 1997).

268   The feitknechtite FTIR spectrum shows OH-related modes similar to those observed for

269   manganite (Fig. 4). Kohler et al. (1997) interpret the broad peak at about 2500 - 2700 cm^{-1} for

270   manganite as arising from OH stretching modes associated with observed H-bonds of ~2.6 Å and

271   assigned the peaks between ~ 900 and 1200 cm^{-1} to OH bending modes. The OH stretch peak for

272   feitknechtite is shifted to a higher frequency (2750 cm^{-1}) relative to that in manganite (2650

273    $cm^{-1)}$, indicating a longer average H-bond (Novak 1974), consistent with our observed value of

274   ~2.80 Å.

275   Our refined occupancies for Mn did not reveal significant vacancy concentrations,

276   although, as discussed below, minor vacancies may give rise to possible superstructures. In the

277   Rietveld refinements, the Mn occupancy factor was strongly correlated with the overall scale

278   factor, making the accurate determination of the Mn occupancy difficult. We have observed

279   similar challenges when trying to determine vacancy concentrations for Mn sites in other Mn

280   oxide layer structures, e.g., birnessite-like phases (unpublished results). Difference Fourier maps

281   calculated during the Rietveld refinements did not show any areas of electron density in the

282   region between the layers that might have corresponded to cations above and below possible

283   octahedral Mn vacancies. Model calculations showed that the refinement is sensitive to the

284   presence of such interlayer cations.

285   The X-ray diffraction patterns showed that all the natural "feitknechtite" samples

286   included some hausmannite, and Rietveld refinements yielded 50 wt%, 30 wt%, and 10 wt%

287   hausmannite in the South Africa, Sweden, and Franklin samples, respectively. Selected area

288   electron diffraction of the South African material suggested that the intergrowth of feitknechtite

289   and hausmannite was topotaxial (Fig. 5AB), with a shared orientation of the 020 planes of

290   hausmannite ($d_{020} = 2.879$ Å) and the $1\bar{1}0$ planes of feitknechtite ($d_{1\text{-}10} = 2.538$ Å). The refined

291   structures for natural feitknechtite samples did not significantly differ from each other or from

292   that of the synthetic sample. The unit-cell parameters showed some slight variation among the

293   natural samples (Table 1), particularly in the *a* and *b* dimensions, especially for the Franklin

294   sample.

295

296   **MnOOH-Phase 2 (ε-MnOOH)**

297   Portehault et al. (2010) derived the same unit-cell parameters as did we for

298   feitknechtite, but they observe that their unit cell "cannot account satisfactorily for feitknechtite

299   because unindexed reflections are still present (e.g., 29.7 and 30.8° on the XRD pattern)". As

300   they used Cu K_{α} radiation ($\lambda = 1.5418$ Å), those peaks correspond to d-spacings of 3.008 and

301   2.903 Å. As described above, we also detected additional peaks in our powder XRD data, albeit

302   in different positions, and we attribute those peaks to a secondary MnOOH phase with a similar

303   unit cell to that of feitknechtite, but with β close to 90° instead of 108.07°. Rietveld analysis

304   indicated that the synthetic feitknechtite contained ~14 wt % of this "MnOOH-Phase 2".

305   Although the closeness in the structures of β-MnOOH and Phase 2 made it difficult to

306   distinguish the two phases by TEM, selected area electron diffraction did reveal a doubling of

307   diffraction spots for both the synthetic and the South African material, indicating epitaxial

308   intergrowths of phases with slightly disparate unit-cell parameters (Fig. 5C). The refinement

309   results in Table 2 and the structure drawing in Figure 3 show that this Phase 2 octahedral Mn^{3+}-O

310   layer structure is nearly identical to that of feitknechtite, but adjacent layers are stacked directly

311   above each other, as in pyrochroite, without an offset along a (Figure 6). The calculated Mn-O

312   bond distances revealed a strong Jahn-Teller type distortion, confirming that the Mn is

313   predominantly trivalent, but the mean Mn-O distance of 1.98 Å is shorter than the value for

314   <Mn-O> of 2.05 Å observed in feitknechtite. Nevertheless, the ratio of the axial-to-equatorial

315   octahedral Mn-O bond lengths was 1.18 for both phases. The difference in mean bond lengths

316   might not be significant as the small fraction of Phase 2 in the sample challenged the

317   determination of accurate atom positions. If the shorter mean Mn-O bond distance in Phase 2

318   was correct, however, it might indicate the presence of some Mn^{4+} in the octahedral site, with

319   charge balance maintained by the replacement of some OH^- by O^{2-}. As the synthetic

320   feitknechtite was formed by reacting hexagonal birnessite (predominantly Mn^{4+}) with aqueous

321   Mn^{2+}, it is possible that Phase 2 represents an intermediate, or second, phase with some remnant

322   Mn^{4+}. To our knowledge, Phase 2 is a previously unreported polymorph of MnOOH, and we

323   propose the designation ε-MnOOH (epsilon-MnOOH) to distinguish from other reported

324   MnOOH polymorphs.

325   The octahedral sheet stacking relationship between feitknechtite and ε-MnOOH is

326   approximately the same as that between triclinic and hexagonal birnessite structures (Fig. 7). In

327   hexagonal birnessite, octahedral (Mn^{4+}, Mn^{3+})-O sheets, with predominantly Mn^{4+}, stack

328   vertically to yield a structure with $P\bar{3}$ symmetry, which can also be described as an

329   orthohexagonal $C2/m$ unit cell with β = 90°. The unit cell for ε-MnOOH is similar to the

330   orthohexagonal cell; β is near 90°, but the a/b ratio is 1.96, resulting from the Jahn-Teller

331   distorted Mn^{3+} octahedra, compared with 1.73 in trigonal birnessite. The octahedral sites in the

332   structure of triclinic Na-birnessite, with formula $Na_{0.58}Mn_2O_4 \cdot 1.7\ H_2O$ (Post and Veblen 1992),

333   contain approximately 2/3 Mn^{4+} and 1/3 Mn^{3+}. Adjacent octahedral sheets are offset along *a*, as

334   in feitknechtite, and the β angle for Na-birnessite in the pseudo-*C*2/*m* unit cell is ~103° (Post et

335   al. 2003).

336

337   **TEM and SEM analyses of feitknechtite microstructures**

338   The SEM BSE and TEM images of the synthetic feitknechtite sample revealed clusters of

339   ~ 0.3 x 0.5 μm lath-like crystals, oriented at ~120 ° to each other (Fig. 8). Energy-dispersive X-

340   ray analysis showed the presence only of Mn and O. Portehault et al (2004) observed similarly

341   oriented crystal clusters in TEM images of synthetic feitknechtite and proposed that they were

342   twinned crystals formed by the lateral assembly of primary nanorods.

343   The natural samples in the present study appeared fine-grained, with individual

344   crystallites smaller than 0.5 μm, and with a layered texture (Fig. 9), likely pseudomorphed after

345   the original pyrochroite. EDS analyses for these samples showed Mg in addition to Mn and O,

346   and Zn for the Franklin sample. The average cation ratios were $Mn_{0.97}Mg_{.03}$, $Mn_{0.93}Mg_{.07}$, and

347     $Mn_{0.87}Mg_{0.10}Zn_{0.03}$ for the samples from South Africa, Sweden, and Franklin, respectively. The

348   Shannon (1976) ionic radii for Mg^{2+} of 0.86 Å, and for Zn of 0.88 Å, are between those of Mn^{2+}

349   (0.97 Å) and Mn^{3+} (0.785 Å), and therefore, might comfortably substitute for Mn in pyrochroite

350   or feitknechtite, or hausmannite, which is associated with feitknechtite in all the natural samples.

351   Luo et al. (1996) synthesized β-MnOOH with Mg as ~25% of the total cations.

352   Because the hausmannite was finely intermixed with the feitknechtite, it was not possible

353   to determine whether the Mg and Zn were equally distributed between the two phases, or more

354   concentrated in one. Analyses from multiple sites on each sample showed general chemical

355   homogeneity within a given sample. Mg and Zn are not Jahn-Teller cations; therefore, as they

356   replace some of the Mn^{3+} in feitknechtite, the average Mn octahedral distortion will be reduced,

357   with a consequent change in the ratio of the a and b unit cell parameters. The Mn^{3+} octahedral

358   distortion is elongated primarily along a (Fig. 2b), and therefore, one might expect that

359   parameter and the a/b ratio should decrease with the addition of Mg or Zn. In fact, the observed

360   a/b ratios follow that trend, with a/b values of 1.956 for synthetic feitknechtite, which has no Mg

361   or Zn, 1.903 and 1.896, for the Swedish and South African samples with 0.07 and 0.03 Mg per

362   octahedral cation site, respectively, and 1.834 for the Franklin sample with 0.1 Mg and 0.03 Zn

363   per Mn site. It is also possible that the natural samples might have some Mn^{2+}, but with the

364   admixed hausmannite, it is not clear how one might confirm its presence in feitknechtite.

365   The synthetic feitknechtite used in the current study was formed by reacting synthetic

366   hexagonal birnessite, with predominantly Mn^{4+}-octahedral sheets, with aqueous Mn^{2+} solutions.

367   The reduction of Mn^{4+} to Mn^{3+} triggers the transformation from birnessite to feitknechtite. As

368   seen in Figure 10, the resulting lath-like feitknechtite crystals were elongated along $b*$, normal to

369   the direction of the axial Mn-O bonds in the Jahn-Teller distorted Mn^{3+} octahedra, which are

370   parallel to the monoclinic a axis. Preferential growth in the direction of the shorter and stronger

371   equatorial bonds is consistent with periodic bond chain theory (Hartman and Perdok 1955). On

372   the other hand, superperiodicities and lattice disorder are concentrated along a*, likely as the

373   result of localized intergrowths of Phase 2 with feitknechtite. The observed morphology suggests

374   that the hexagonal birnessite crystals templated the growth of the feitknechtite crystals. Because

375   of the trigonal symmetry of the Mn^{4+}-O octahedral sheet in the original birnessite, the newly

376   formed feitknechtite crystals oriented and grew with equal probability in any of three directions

377   at 120 ° to each other.

378   Feitknecht and Marti (1942) and Bricker (1965) synthesized feitknechtite by oxidation of

379     $Mn(OH)_2$ (pyrochroite). Hem (1981) presumes that the similarity of the layer structures of

380   feitknechtite and pyrochroite promotes the transformation from $Mn(OH)_2$ to β-MnOOH. In fact,

381   the natural feitknechtite investigated in the present study formed, with hausmannite, as

382   alterations of pyrochroite, retaining the crystal morphology of the original phase. X-ray

383   diffraction patterns from many of these pseudomorphs show single-crystal spots rather than

384   powder rings, consistent with a transformation that preserved the basic crystal structure.

385   Luo et al. (1998) determined that β-MnOOH is the intermediate phase when $Mn(OH)_2$ is

386   oxidized by dissolved permanganate during the synthesis of birnessite-like phases. We have

387   similarly observed that oxidation of $Mn(OH)_2$ in solution by O_2 initially forms β-MnOOH, which

388   then transforms to a triclinic birnessite phase (unpublished results). As with the case of

389   hexagonal birnessite, the trigonal symmetry of the pyrochroite Mn^{2+}/O octahedral sheets allows

390   monoclinic β-MnOOH crystals to grow equally well in three orientations. TEM and SEM

391   images of synthetic triclinic birnessite crystals (Fig. 9) commonly show sheets constructed of

392   parallel lath-like components, sometimes twinned at 120° angles, which likely reflect the

393   morphologies of the precursor monoclinic β-MnOOH crystals. Similarly, SEM images of the

394   Ca-birnessite-like mineral rancieite (Fig. 9) typically reveal sheet-like crystals that are

395   composites of twinned lath-like components, despite their overall trigonal ($P\overline{3}$) symmetry (Post

396   et al. 2008). Rancieite is most typically found in the oxidation zones of Mn-rich deposits or in

397   low-temperature mineralized veins and vugs in limestone (Ertle et al. 2005). It seems reasonable

398   that the twinned, lath-like crystal morphology reflects pseudomorphic alteration from

399   feitknechtite, which in turn transformed from pyrochroite.

400

Thermal transformation of β-MnOOH (feitknechtite) to hausmannite

When synthetic β-MnOOH was heated from 25 °C to ~200 °C, the structure showed a small but continuous thermal expansion (Fig. 11), with an increase in unit-cell volume of 0.5%. The dependence of the unit-cell parameters on temperature (Figure 11) reveals that most of the expansion occurred along the a direction (+0.3%), which is the direction of the longer axial Mn^{3+}-O octahedral bonds. Over this temperature range, the changes in the individual b, c, and β unit-cell parameters were 0.1% or less. Between ~200 and 230 °C, the transformation of feitknechtite to hausmannite was marked by a decrease in unit-cell volume by ~1%, mostly caused by ~0.3% contractions in the a and b parameters. Hausmannite was first detected in the diffraction pattern at 226 °C, and feitknechtite was absent by 244 °C. The Rietveld refinement for the diffraction pattern collected at 235 °C determined the sample was 82% hausmannite and 18% feitknechtite. Our results are consistent with TGA measurements (Yan et al. 1998), which showed an abrupt weight loss for β-MnOOH at ~225 °C. The X-ray diffraction data revealed no evidence for an intermediate amorphous phase. The transformation of feitknechtite to hausmannite requires loss of OH (as H_2O) and reduction of 1/3 of the Mn^{3+} to Mn^{2+}, according to the reaction:

$$3Mn^{3+}OOH \rightarrow Mn^{3+}_2Mn^{2+}O_4 + 3/2H_2O + 1/4O_2 \qquad (1)$$
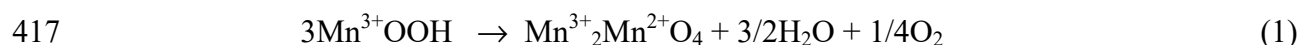
The displacement of some of the Mn^{3+} and all of the newly reduced Mn^{2+} from the feitknechtite octahedral sheets to the interlayer region builds the hausmannite spinel structure (Fig. 12). Bricker (1965) concludes that hausmannite is a more stable phase than feitknechtite, but only slightly so. Interestingly, the reported transformation temperature for the dehydration of FeOOH (goethite) to Fe_2O_3 (hematite) also is in the range of 240-255 °C (Özdemir and Dunlop,

423   2000). In both cases, the trigger for the transformation is loss of OH, accompanied by the

424   reduction of some Mn in feitknechtite.

IMPLICATIONS

426   This study provides the first complete structure description for β-MnOOH (feitknechtite).

427   Additionally, we identified and report the structure for a second MnOOH phase (ε-MnOOH),

428   similar to β-MnOOH but with a different layer stacking, and as such seems to be a new MnOOH

429   polymorph. Several researchers have described feitknechtite as a requisite intermediate phase

430   during the synthesis of technologically important Mn (hydr)oxides. It is also assumed to play a

431   critical role in abiotic and biotic processes that produce and alter Mn oxide phases in a variety of

432   natural environments. The lack of knowledge of the atomic structure of feitknechtite has limited

433   our understanding of its precise role and behavior in synthetic and natural redox reactions in

434   manganiferous systems. Our work provides the formal structure description required for model

435   calculations that will provide a better understanding of this phase, and make possible predictions

436   about the behavior of β-MnOOH (feitknechtite) under a range of conditions. It also provides an

437   essential starting point for analyzing powder diffraction data to determine and monitor unit-cell

438   parameters and other structure details, and for quantitative phase analyses of Mn oxide samples

439   that contain feitknechtite. Feitknechite has been part of the Mn oxide conversation for more than

440   seven decades, and it is satisfying to finally know what it is.

441

442

443

ACKNOWLEDGEMENTS

444

453   **REFERENCES**

454   Aminoff, G. (1919). Über die Krystallstruktur des Pyrochroits. Geologiska Föreningen i

455   Stockholm Förhandlingar, *41*(5), 407-431.

456   Baron, V., Gutzmer, J., Rundlo, H., Tellgren, R., 1998. The influence of iron substitution

457   on the magnetic properties of hausmannite, $Mn^{2+}(Fe,Mn)_2^{3+}O_4$. American Mineralogist 83,

458   786–793.

459   Baur, W.H. (1972) Prediction of hydrogen bonds and hydrogen atom positions in

460   crystalline solids. Acta Crystallographica, B28, 1456-1465

461   Bargar, J.R., Tebo, B.M., Bergmann, U., Webb, S.M., Glatzel, P., Chiu, V.Q., Villalobos,

462   M., 2005. Biotic and abiotic products of Mn(II) oxidation by spores of the marine Bacillus sp.

463   strain SG-1. American Mineralogist 90, 143–154.

464   Bricker, O. (1965) Some stability relations in the system $Mn-O_2-H_2O$ at 25° and one

465   atmosphere total pressure. American Mineralogist, 50, 1296-1354.

466   Chukanov, N.V., Varlamov, D.A., Pekov, I.V., Zubkova, N.V., Kasatkin, A.V., and

467   Britvin, S.N. (2021) Coupled Substitutions in Natural MnO(OH) Polymorphs: Infrared

468   Spectroscopic Investigation Infrared Spectroscopic Investigation. Minerals, 11, 969-981.

469   Elzinga, E.J. (2011) Reductive transformation of birnessite by aqueous Mn(II).

470   Environmental Science and Technology, 45, 6366-6372.

471   Ertl, A., Pertlik, F., Prem, M., Post, J.E., Kim, S.J., Brandstätter, F., and

472   Schuster, R. **2005**. "Ranciéite Crystals from Friesach, Carinthia, Austria," Eur. J. Mineral. **17**,

473   163–172.

474   Feitknecht, V.W. and Marti, W. (1945) Über die Oxydation von Mangan(II)-hydroxyd

475   mit molekularem Sauerstoff. Helvetica chimica Acta, 28, 129-148.

476   Feitknecht, V.W., Brunner, P., and Ostwald, H.R. (1962) Über den einfluß der

477   feuchtigkeit auf die oxydation von manganhydroxid durch molekularen sauerstoff. Zeitschrift

478   für anorganische und allgemeine Chemie, 316, 154-160.

479   Frondel, C. (1953) New manganese oxides: hydrohausmannite and woodruffite.

480   American Mineralogist, 38, 761-769.

481   Grangeon, S., Warmont, F., Tournassat, C., Lanson, B., lanson, M., Elkaim, E., and

482   Claret, F. (2017) Nucleation and growth of feitknechtite from nanocrystalline vernadite

483   precursor. European Journal of Mineralogy, 29, 767-776.

484   Hartman, P., and Perdok, W. G. (1955). On the relations between structure and

485   morphology of crystals. I., Acta Crystallographica, 8, 49-52.

486   Hem, J. D. (1978) Redox processes at surfaces of manganese oxide and

487   their effects on aqueous metal ions, Chemical Geology, 21, 199-218.

488   Hem, J. D. (1981) Rates of manganese oxidation in aqueous systems. Geochimica et

489   Cosmochimica Acta, 45, 1369-1374

490   Hem, J.D., Roberson, C.E., and Fournier, R. (1982) Stability of βMnOOH and

491   manganese oxide deposition from springwater. Water Resources Research, 18, 563-570.

492   Ilton, E.S., Post, J.E., Heaney, P.J., Ling, F.T. and Kerisit, S.N. (2016) XPS

493   determination of Mn oxidation states in Mn (hydr) oxides. Applied Surface Science, 366, 475-

494   485.

495   Klewicki, J.K., and Morgan, J.J. (1999) Dissolution of β-MnOOH particles by ligands:

496   pyrophosphate, ethylenediaminetetraacetate, and citrate. Geochimica et Cosmochimica Acta, 63,

497   3017-3024.

498   Kohler, T., Armbruster, T.A., and Libowitzky, E. (1997) Hydrogen bonding and Jahn–

499   Teller distortion in groutite, a-MnOOH, and manganite, γ-MnOOH, and their relations to the

500   manganese dioxides ramsdellite and pyrolusite. Journal of Solid State Chemistry, 133, 486-500.

501   Lefkowitz, J.P., Rouff, A.A., and Elzinga, E.J. (2013) Influence of pH on the reductive

502   transformation of birnessite by aqueous Mn(II). Environmental Science & Technology, 47(18),

503   10364-71.

504   Luo, J., Segal, S.R., Wang, J.Y., Tian, Z.R., and Suib, S.L. (1996) Synthesis,

505   characterization, and reactivity of feitknechtite. Materials Research Society Symposium

506   Proceeding, 431, 3-8.

507   Luo, J., Huang, A., Park, S.H., Suib, S.L., and O'Young, C. (1998) Crystallization of

508   Sodium-birnessite and accompanied phase transformation. Chemistry of Materials, 10, 1561-

509   1568.

510   Mandernack, K.W., Post, J.E., Tebo, B.M., 1995. Manganese mineral formation by

511   bacterial spores of a marine Bacillus, strain SG-1: Evidence for the direct oxidation of Mn(II) to

512   Mn(IV). Geochimica et Cosmochimica Acta 59, 4393–4408.

513   Meldau, R., Newesely, H., and Strunz, H. (1973) Zur kristallchemie von feitknechtite, β-

514   MnOOH. Naturwissenschaften, 60, 387.

515   Novak, A. (1974) Hydrogen bonding in solids correlation of spectroscopic and

516   crystallographic data. Structure and Bonding 18, 177—216

517   Özdemir, Ö and Dunlop, D.J. (2000) Intermediate magnetite formation during

518   dehydration of goethite. Earth and Planetary Science Letters, 177, 59-67.

519   Portehault, D., Cassaignon, S., Baudrin, E., and Jolivet, J (2010) Evolution of

520   nanostructured manganese (oxyhydr)oxides in water through MnO_4^- reduction. Crystal Growth

521   & Design, 10, 2168-2173.

522   Post, J.E. and Bish, D.L. (1989) Rietveld refinement of crystal structures using

523   powder X-ray diffraction data. In D.L. Bish and J.E. Post, Eds., Reviews in Mineralogy: Modern

524   Powder Diffraction, 20, 277–308. The Mineralogical Society of America, Washington, D.C

525   Post, J.E., and Veblen, D.R. (1990) Crystal structure determinations of synthetic sodium,

526   magnesium, and potassium birnessite using TEM and the Rietveld method. American

527   Mineralogist, 75, 477-489.

528   Post, J.E., Heaney, P.J., and Hanson, J. (2002) Rietveld refinement of a triclinic structure

529   for synthetic Na-birnessite using synchrotron powder diffraction data. Powder Diffraction, 17(3),

530   218-221.

531   Post, J.E., Heaney, P.J., and Ertl, A. (2008) Rietveld refinement of the ranciéite structure

532   using synchrotron powder diffraction data. Powder Diffraction, 23(01), 10-14.

533   Prescher, C, and Prakapenka, V. B. (2015) "DIOPTAS: A Program for Reduction of

534   Two-Dimensional X-Ray Diffraction Data and Data Exploration." High Pressure Research, 35,

535   223–30.

536   Rietveld, H.M. (1969) A Profile Refinement Method for Nuclear and Magnetic

537   Structures. Journal of Applied Crystallography, 2(2), 65-71.

538   Thompson, P., Cox, D.E., and Hastings, J.B. (1987) Rietveld refinement of Debye-

539   Scherrer synchrotron X-ray data from Al_2O_3. Journal of Applied Crystallography, 20, 79–83.

540   Toby, B.H., and Von Dreele, R.B. (2013) GSAS-II: the genesis of a modern open-source

541   all purpose crystallography software package. Journal of Applied Crystallography, 46(2), 544-

542   549.

543   Shannon, R.D. (1976) Revised Effective Ionic Radii and Systematic Studies of

544   Interatomie Distances in Halides and Chaleogenides. Acta crystallographica. Section A,

545   Foundations of crystallography 32, 751-767.

546   Stephens, P.W. (1999) Phenomenological model of anisotropic peak broadening in

547   powder diffraction. Journal of Applied Crystallography, 32, 281–289.

548

549   Yan, D., Li, Y., Liu, Y., Zhuo, R., Wu, R., and Wang, J. (2014) Growth mechanism and

550   morphology control of porous hexagonal plates of hydrohausmannite prepared by hydrothermal

551   method. Applied Mechanics and Materials, 513-517, 277-280.

552

553   Yamamoto, N., Horibe, M., and Higashi, S. (1981) Fourth polymorph of MnOOH; δ-

554   MnOOH. Journal of the Japan Society of Powder and Powder Metallurgy, 28, 282-285.

555

556

557   **FIGURE CAPTIONS**

558

559   **Figure 1.** Final Rietveld observed (blue crosses), calculated (solid green) and difference (light

560   blue) powder diffraction patterns for β-MnOOH and phase 2 MnOOH. The blue marker lines

561   indicate positions for the indexed peaks, and the refined background is shown as the solid red

562   line. $\lambda = 0.414211$ Å.

563

564   **Figure 2.** Observed (black) and modeled (red) selected area electron diffraction patterns for

565   synthetic β-MnOOH along the following zone axes: A) [001]; B) [112]; and C) [110].

566

567   **Figure 3.** Polyhedral drawing of the β-MnOOH (feitknechtite) structure looking A) along

568   *b*, and B) along *c*, and C) for MnOOH-Phase 2 along *b*. The Mn^{3+}-O octahedra are shown in red,

569   and the O/OH positions are plotted as blue spheres. The unit-cells are indicated by dashed lines.

570

571   **Figure 4.** FTIR spectra for synthetic feitknechtite (lower) and manganite (upper).

572

573   **Figure 5.** A) Unlabeled SAED pattern for South African sample showing doubled spots

574   indicative of topotaxial intergrowth of feitknechtite and hausmannite. B) Simulated SAED

575   patterns for feitknechite along ZA [001] (red) and for hausmannite along ZA [$\bar{2}$01] (blue),

576   superimposed on the above pattern. C) SAED pattern for synthetic β-MnOOH (ZA [001])

577   revealing a slight doubling of diffraction spots (arrowed), suggestive of the intergrowth of

578   feitknechtite and Phase-2.

579   **Figure 6.** Polyhedral structure representation of MnOOH-Phase 2 (A and B) and pyrochroite (C

580   and D), projected parallel and normal to the octahedral layers. The Mn-O octahedra are shown in

581   red, and the O,OH atoms are dark blue spheres.

582

583   **Figure 7.** Polyhedral structures, parallel to the layers, comparing A) feitknechtite and B)

584   MnOOH-Phase 2 to C) triclinic birnessite (interlayer cations and water molecules omitted) and

585   D) hexagonal birnessite (interlayer cations and water molecules omitted). The Mn-O octahedra

586   are shown in red, and the O,OH atoms are dark blue spheres.

587

588   **Figure 8**. A) SEM BSE image of β-MnOOH, B) SEM BSE image of feitknechtite from South

589   Africa, C) TEM image of synthetic β-MnOOH, and D) TEM image of feitknechtite from South

590   Africa.

591

592   **Figure 9.** A) TEM image of synthetic Na-birnessite, B) SEM BSE image of rancieite from

593   Alsace, France, C) and D) SEM BSE images of rancieite from Spain.

594

595   **Figure 10.** A) HRTEM image of β-MnOOH lath with fast Fourier transform (inset) reveals that

596   crystals are elongate along the b^* direction, with local superperiodicities and lattice disorder

597   along the a^* direction. B) Higher magnification HRTEM image reveals significant disorder

598   along a^*, the direction of elongated Mn^{3+}-O bonds due to Jahn-Teller distortions.

599   **Figure 11**. Temperature dependence of a (top) and unit-cell volume (bottom) for β-MnOOH.

600

601   **Figure 12.** Polyhedral structural representation of transformation of β-MnOOH (left) to

602   hausmannite (right) above ~225 °C. The Mn^{3+}-O octahedra are shown in red, the Mn^{2+}-O

603   tetrahedra in light blue, and the O,OH (β-MnOOH) and O (hausmannite) atoms as dark blue

604   spheres.

605

30

606

607   **TABLES**

608   **Table 1.** Rietveld Refined Unit-cell parameters ($C2/m$) for β-MnOOH (Feitknechtite) and
609   MnOOH-Phase2, and synthetic Na-birnessite (P-1)
610

Sample	a (Å)	b (Å)	c (Å)	α (°)	β (°)	γ (°)
β-MnOOH	5.6541(4)	2.89075(2)	4.8347(3)		108.0709(1)	
Impurity phase	5.6509(1)	2.89072(4)	4.6025(1)		89.976(6)	
South Africa	5.523(1)	2.901(1)	4.866(1)		108.44(1)	
Sweden	5.501(1)	2.902(1)	4.847(1)		108.58(1)	
Franklin, NJ	5.382(1)	2.934(1)	4.886(1)		108.86(1)	
Na-birnessite[*]	5.1746(2)	2.8474(1)	7.3319(4)	89.444(5)	103.181(4)	89.948(6)

611   *Post et al. (2002)

612

613   **Table 2.** Atomic coordinates and selected bond distances (Å) for β-MnOOH (feitknechtite) and
614   MnOOH-Phase 2

615

Feitknechtite					
Atom	x	y	z	Site occupancy Factor	U_{iso}
Mn	0	0	0	1.0	0.0066(2)
O	0.4206(2)	0	0.2217(2)	1.0	0.00227(2)

616

Mn-O	2.2856(8) (x2)
	1.9333(6) (x4)
<Mn-O>	2.05
O-O	2.800(2) (x2)
O-O	2.568(2)
O-O	2.559(2)

MnOOH-Phase 2					
Atom	x	y	z	Site occupancy Factor	${}^{*}U_{iso}$
Mn	0	0	0	1.0	0.005
O	0.3579(6)	0	0.191(1)	1.0	0.005

Mn-O	2.206(4) (x2)
	1.872(3) (x4)
<Mn-O>	1.98
O-O	2.891 (x2)
O-O	2.380(8)
O-O	2.583(8) (x2)

617   Note: esd's are those reported from the Rietveld refinement, and previous studies indicate might
618   be underestimated by an order of magnitude, or more (Post and Bish, 1989)
619   * Temperature factors were held fixed to values given
620

FIGURES
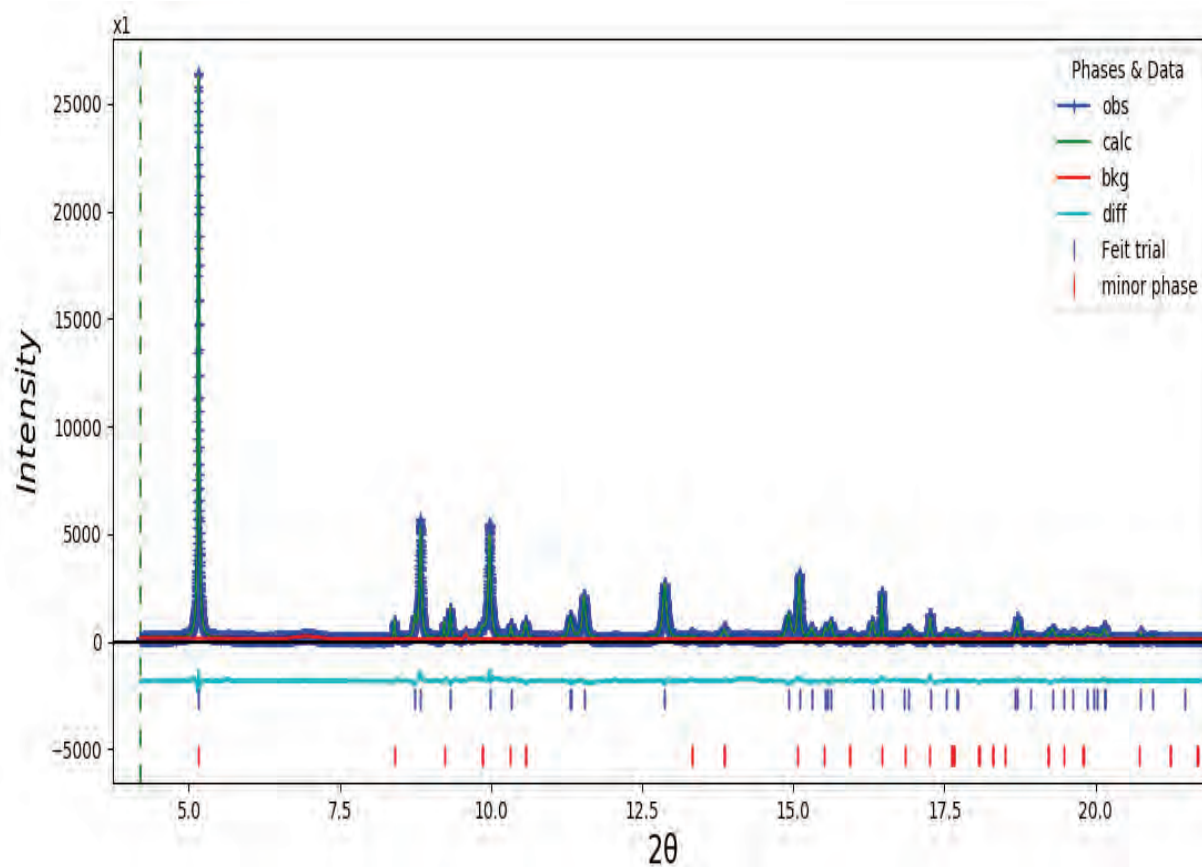
Figure 1. Final Rietveld observed (blue crosses), calculated (solid green) and difference (light-blue) powder diffraction patterns for β-MnOOH and phase 2 MnOOH. The blue marker lines indicate positions for the indexed peaks, and the refined background is shown as the solid red line.

c.
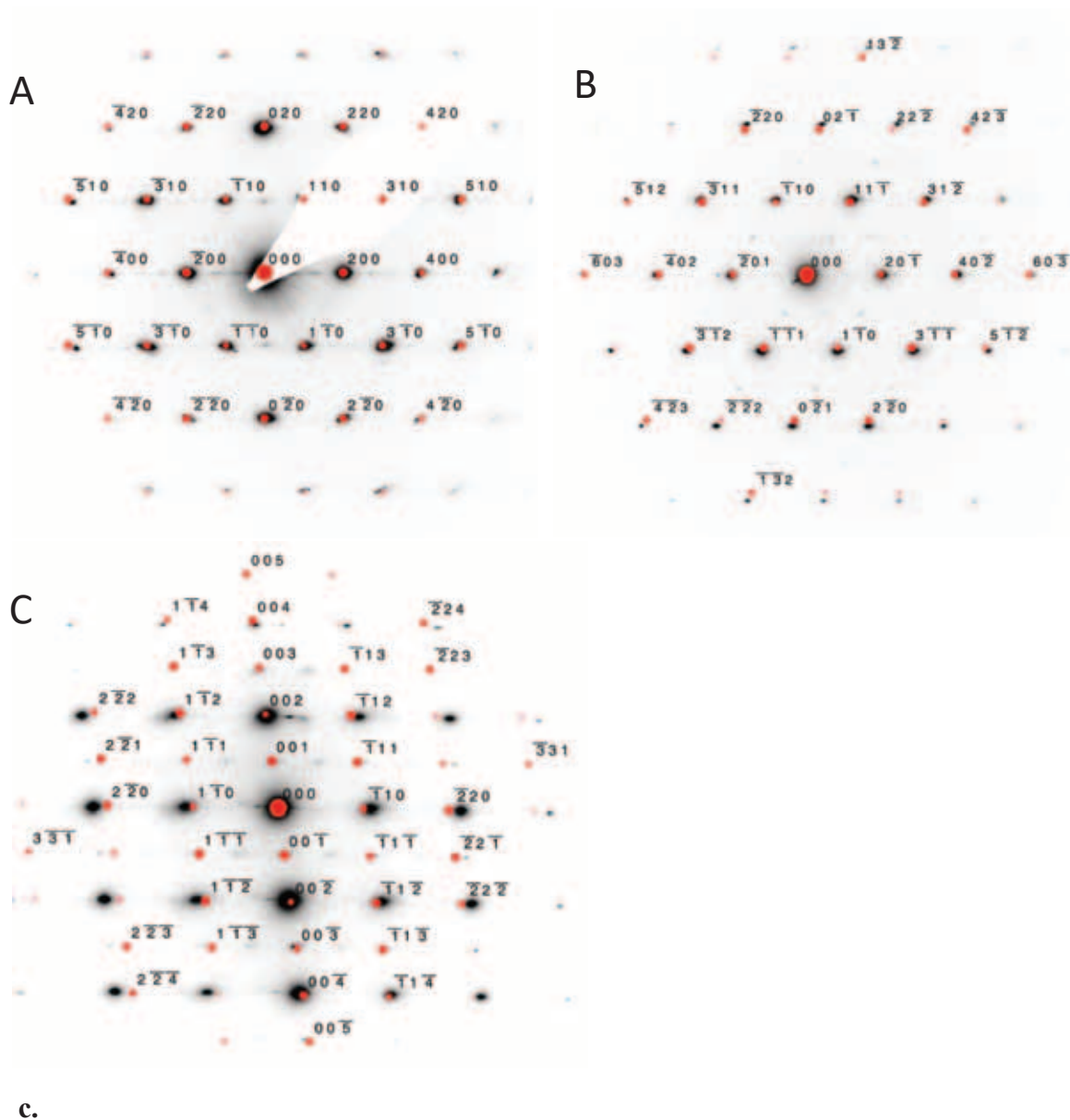
Figure 2. Observed (black) and modeled (red) selected area electron diffraction patterns for synthetic β-MnOOH along the following zone axes: A) [001]; B) [112]; and C) [110].
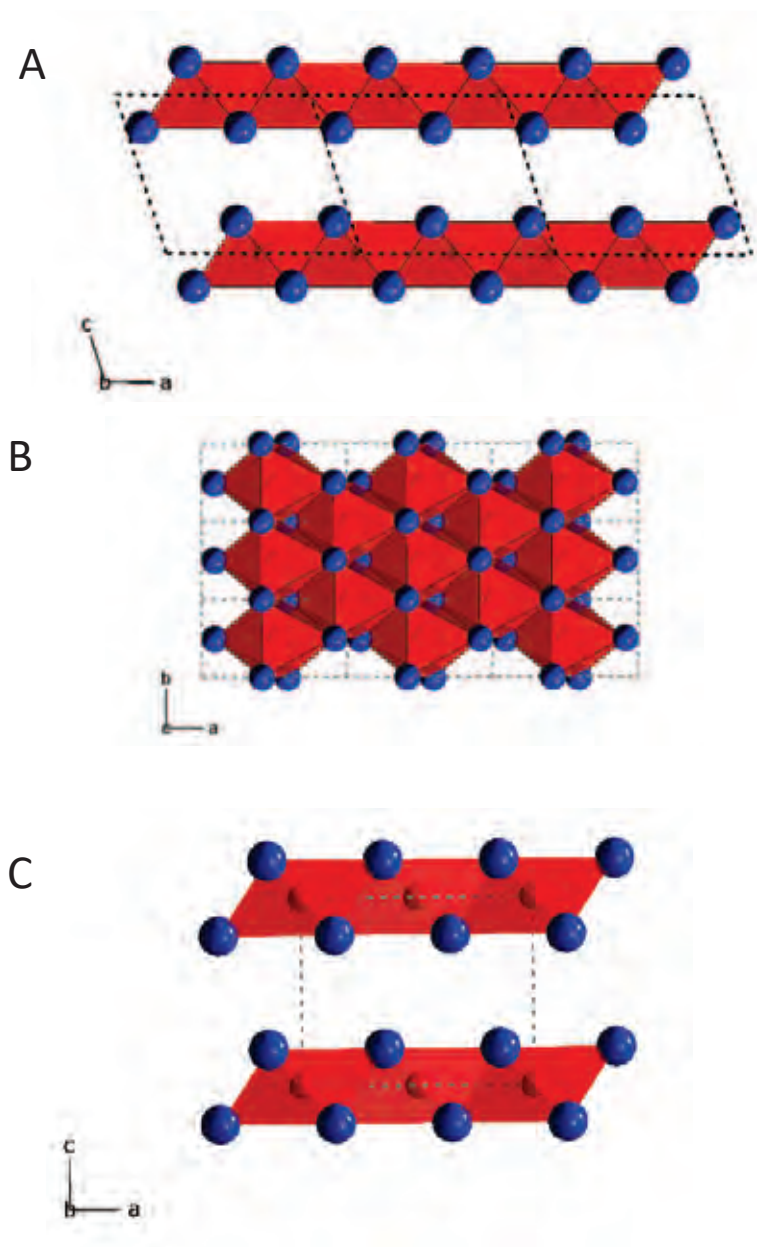
Figure 3. Polyhedral drawings of the β-MnOOH (feitknechtite) structure looking A) along

b and B) along c. C) Structure for MnOOH-Phase 2 along b. The Mn^{3+}-O octahedra are shown

in red, and the O/OH positions are plotted as blue spheres. The unit-cells are indicated by

dashed lines.
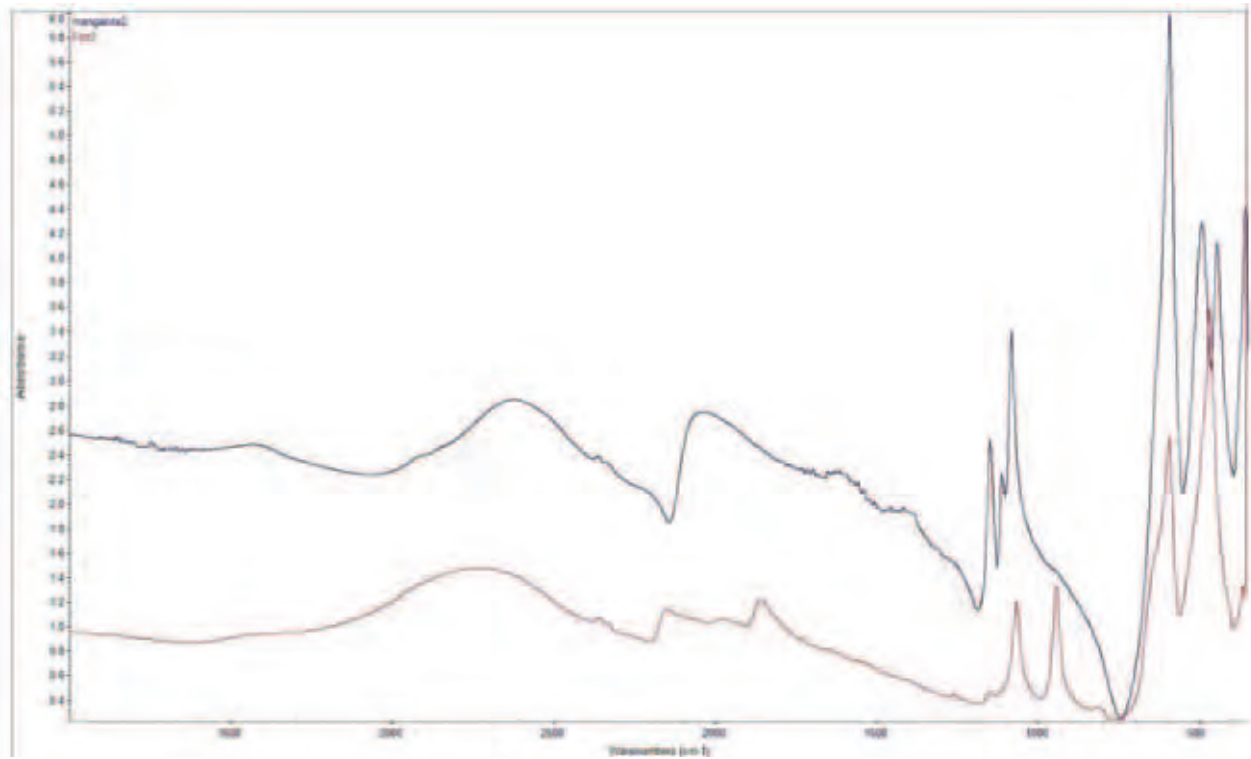
Figure 4. FTIR spectra for synthetic feitknechtite (lower) and manganite (upper).
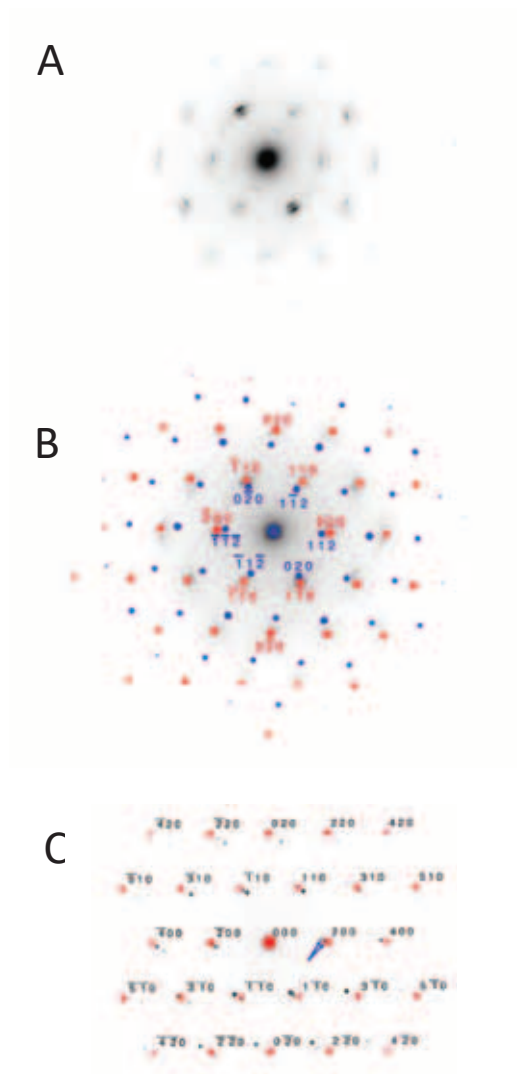
Figure 5. A) Unlabeled SAED pattern for South African sample showing doubled spots indicative of topotaxial intergrowth of feitknechtite and hausmannite. B) Simulated SAED patterns for feitknechite along ZA [001] (red) and for hausmannite along ZA [$\bar{2}$01] (blue), superimposed on the above pattern. C) SAED pattern for synthetic β-MnOOH (ZA [001]) revealing a slight doubling of diffraction spots (arrowed), suggestive of the intergrowth of feitknechtite and Phase-2.
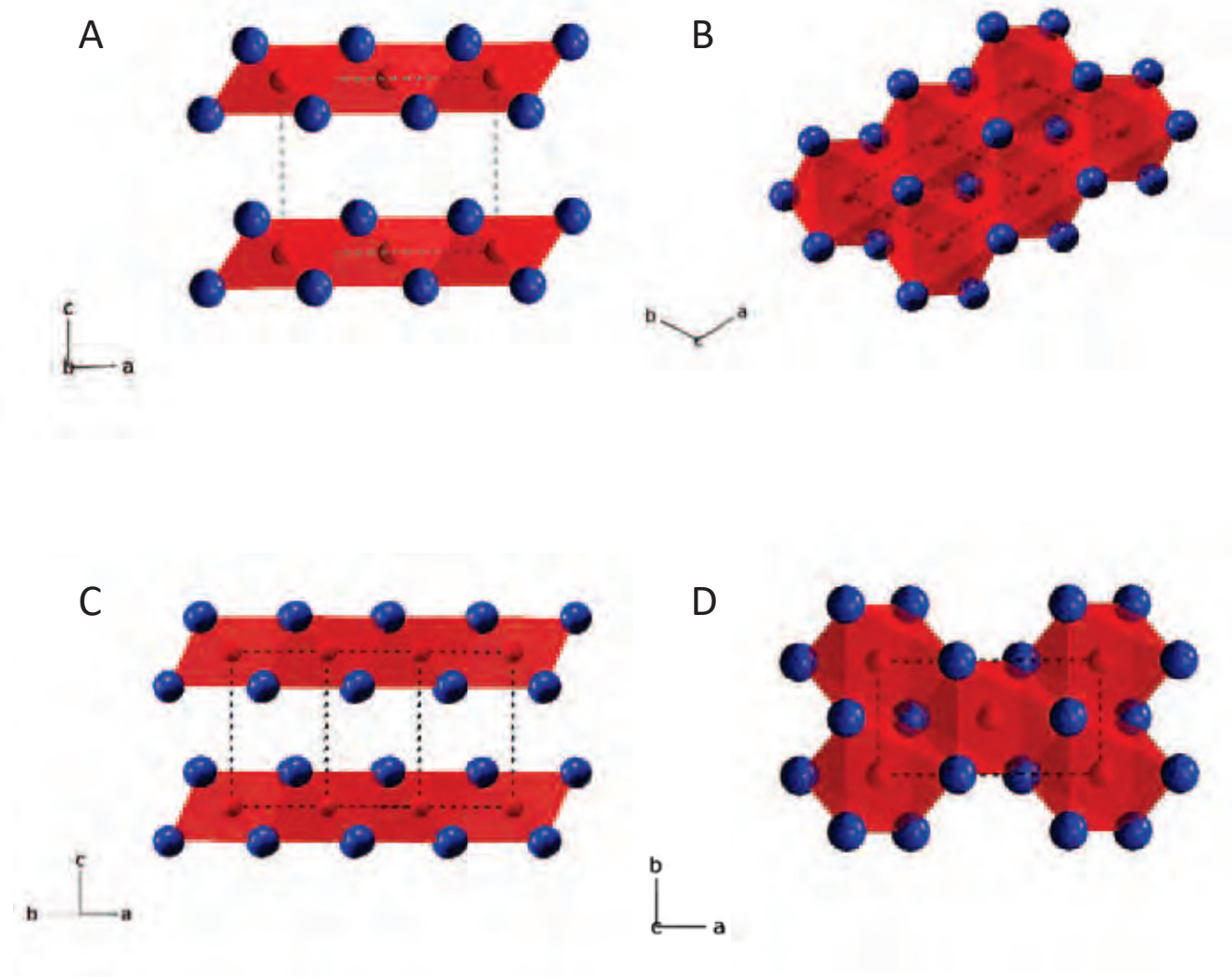
Figure 6. Polyhedral structure representation of pyrochroite (A and B) and MnOOH-Phase 2 (C

and D), projected parallel and normal to the octahedral layers. The Mn-O octahedra are shown in

red, and the O,OH atoms are dark blue spheres.
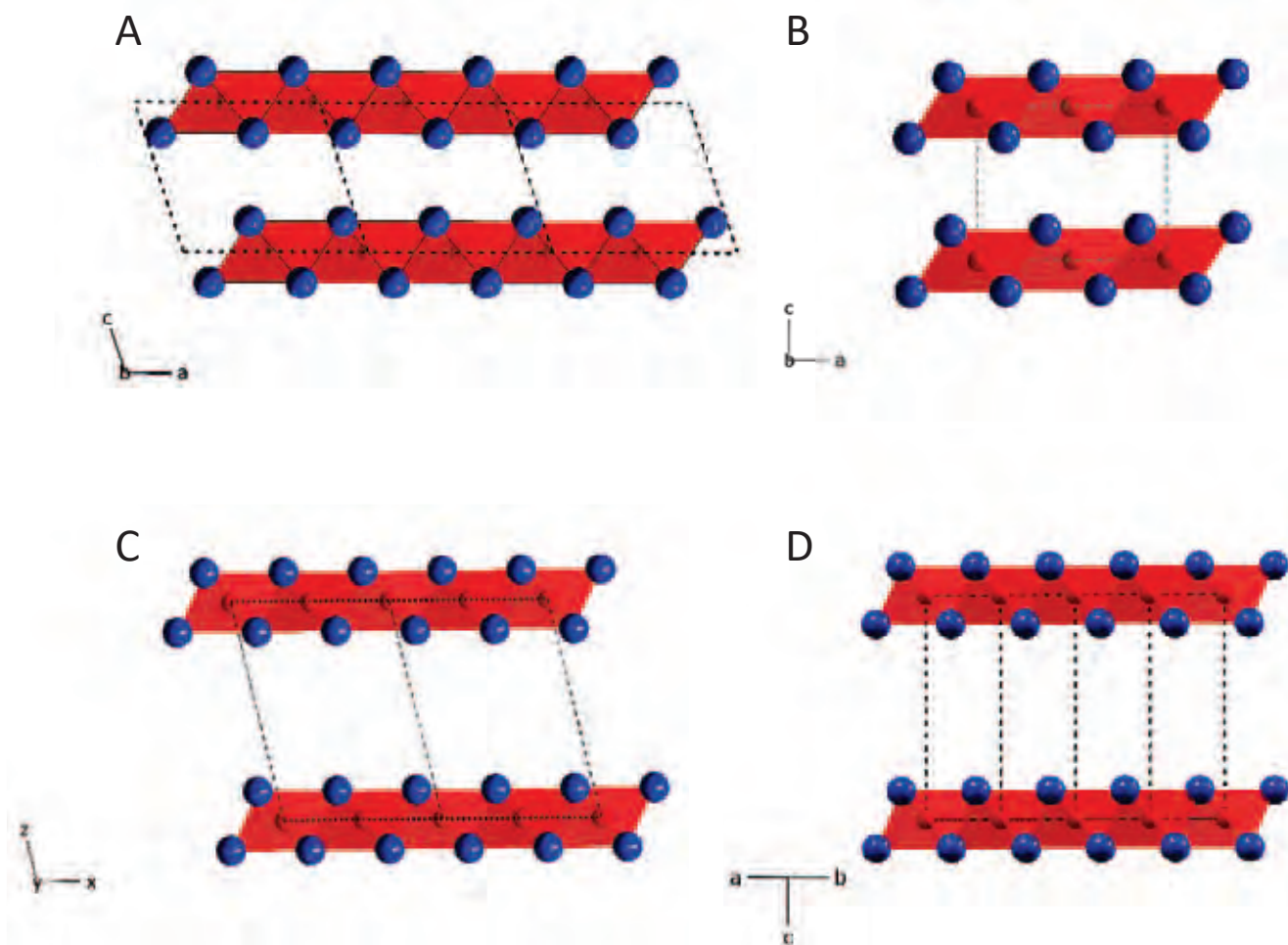
Figure 7. Polyhedral structures, parallel to the layers, comparing A) feitknechtite and B)

MnOOH-Phase 2 to C) triclinic birnessite (interlayer cations and water molecules omitted) and

D) hexagonal birnessite (interlayer cations and water molecules omitted). The Mn-O octahedra

are shown in red, and the O,OH atoms are dark blue spheres.
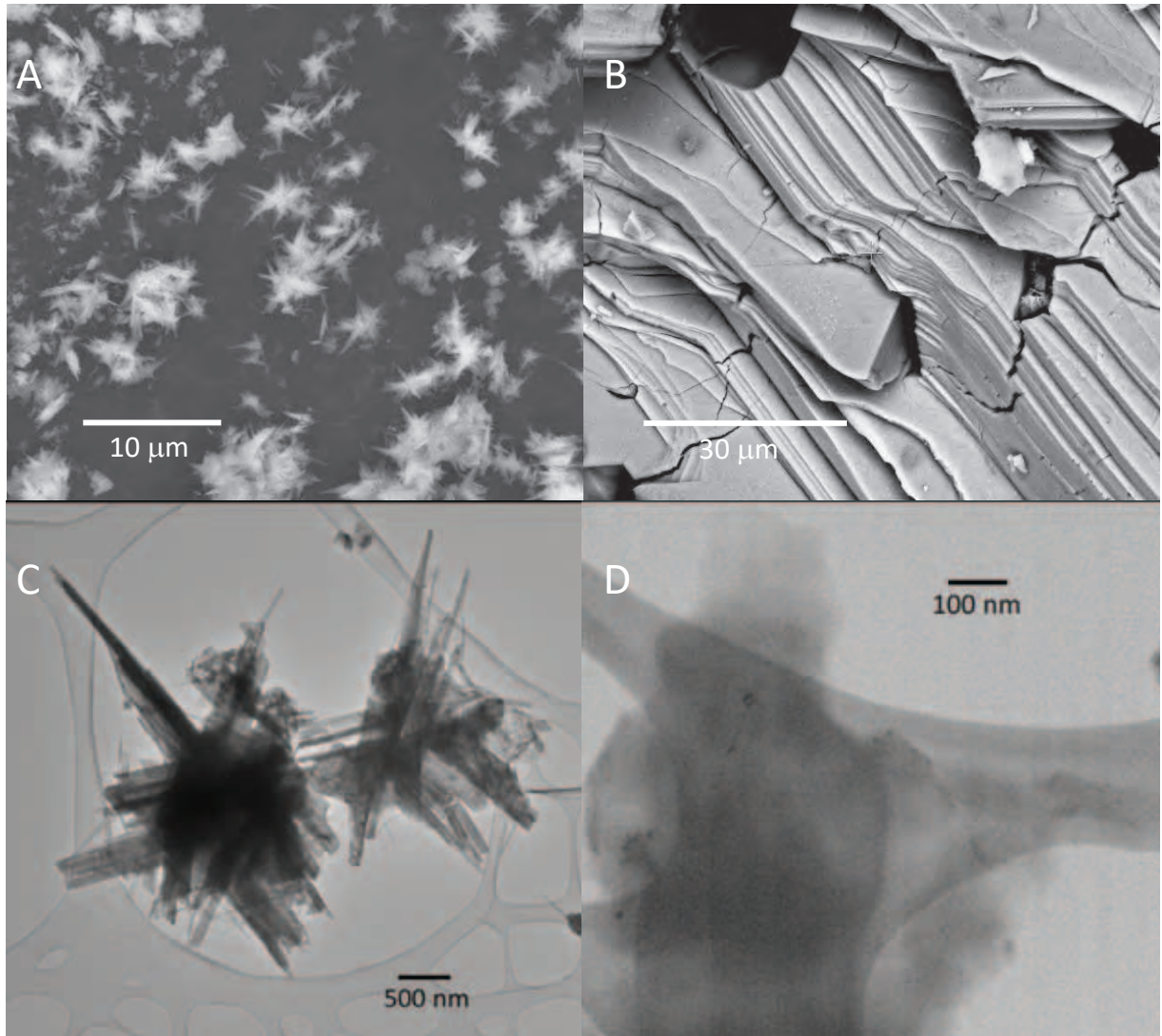
Figure 8. A) SEM BSE image of β-MnOOH, B) SEM BSE image of feitknechtite from South

Africa, C) TEM image of synthetic β-MnOOH, and D) TEM image of feitknechtite from South

Africa.
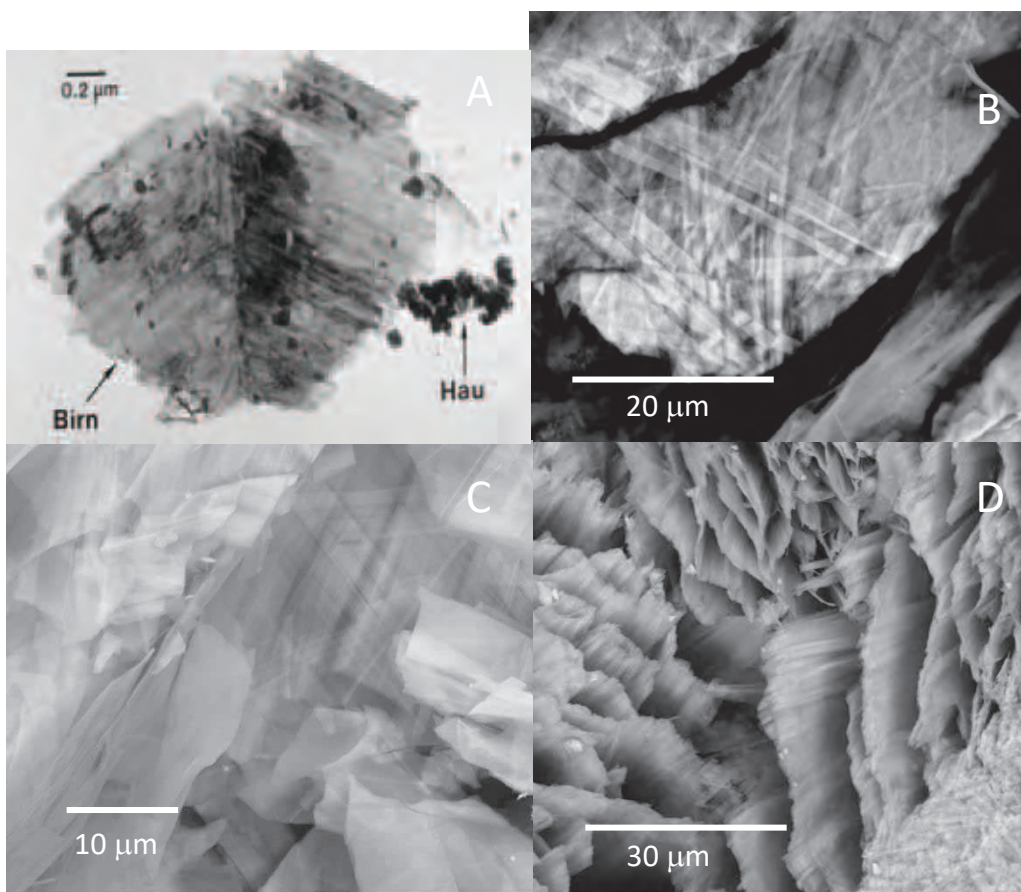
Figure 9. A) TEM image of synthetic Na-birnessite (Birn) with hausmannite (Hau), B) SEM

BSE image of rancieite from Alsace, France, C) and D) SEM BSE images of rancieite from

Spain.
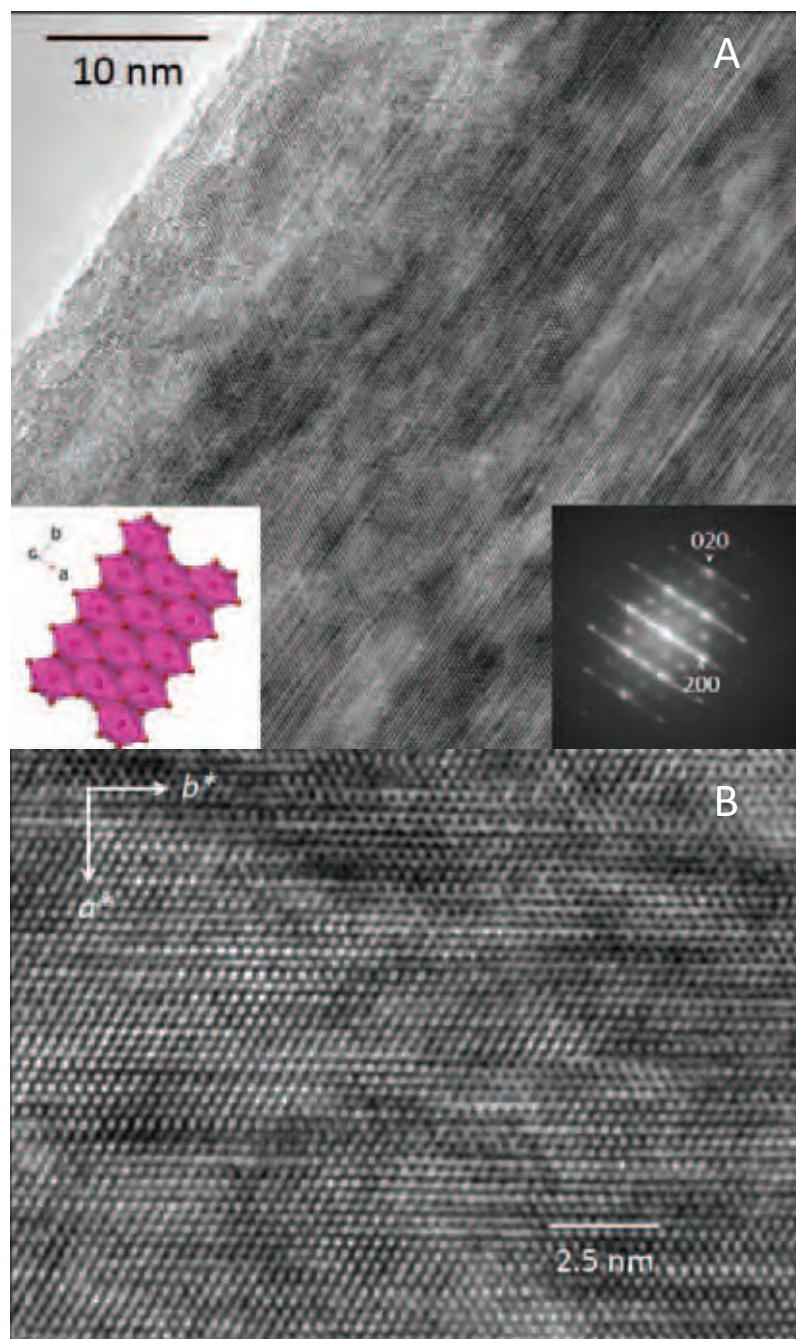
Figure 10. A) HRTEM image of β-MnOOH lath with fast Fourier transform (inset) reveals that crystals are elongate along the $b*$ direction, with local superperiodicities and lattice disorder along the $a*$ direction. B) Higher magnification HRTEM image reveals significant disorder along $a*$, the direction of elongated Mn^{3+}-O bonds due to Jahn-Teller distortions
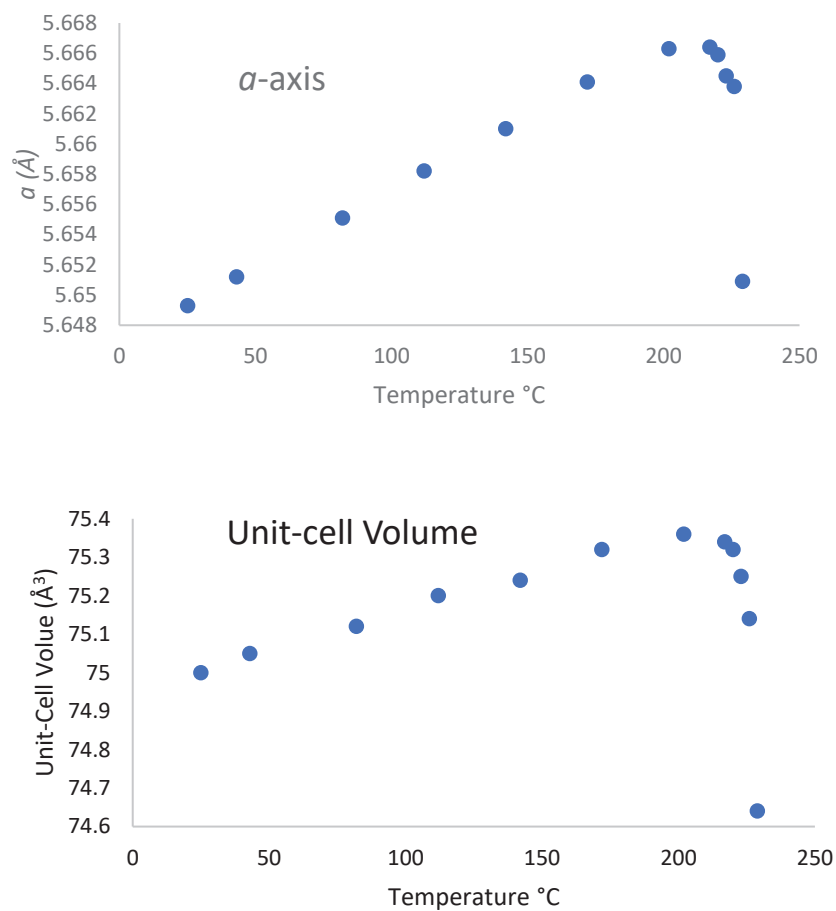
Figure 11. Temperature dependence of a (top) and unit-cell volume (bottom) for β-MnOOH.
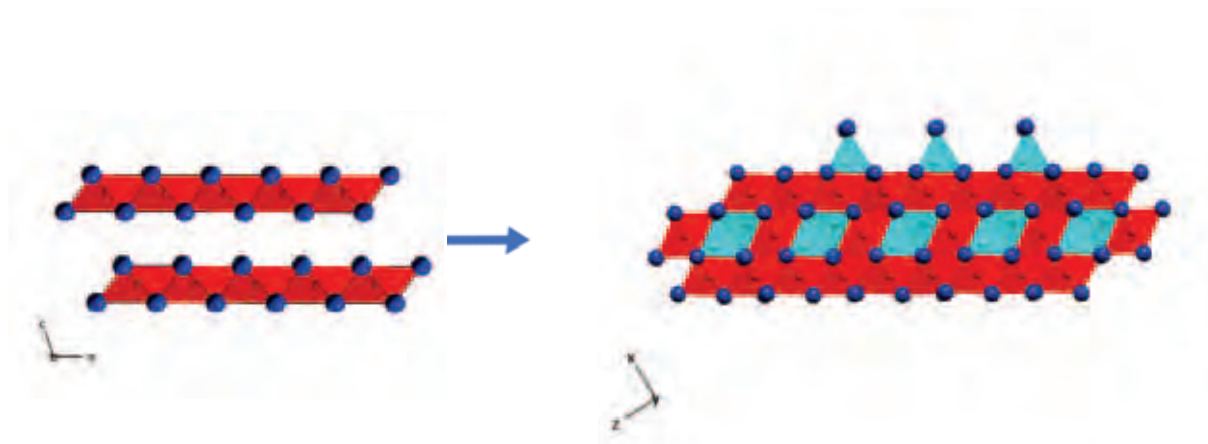
Figure 12. Polyhedral structural representation of transformation of β-MnOOH (left) to hausmannite (right) above ~225 °C. The Mn^{3+}-O octahedra are shown in red, the Mn^{2+}-O tetrahedra in light blue, and the O,OH (β-MnOOH) and O (hausmannite) atoms as dark blue spheres.